Supplementary Material: Generation of wave turbulence in dipolar gases driven across their phase transitions

SUPPLEMENTARY NOTE 1: DYNAMICS IN THE AXIAL DIRECTION

In the main text, the dynamics of the planar density is tracked, revealing the emergence of a non-equilibrium quasi-steady state at long evolution times. Due to the considered trap aspect ratio ($\omega_z/\omega_r = 3$) though, the dynamics cannot be considered as purely 2D, since the transverse excitation energy is smaller than the chemical potential of the initial state, i.e. $\hbar\omega_z < \mu$. It is therefore rather a quasi-2D setup in the sense that the high-density droplet crystals are arranged in the plane, setting also a characteristic momentum scale, the roton momentum. To appreciate the dynamics in the z direction in the case of the supersolid-to-superfluid crossing, the integrated density $n(z,t) = \int dxdy\ |\Psi(x,y,z,t)|^2$ is monitored, see Fig. S1(a). As time evolves, it becomes apparent that the density $n(z,t)$ features a relatively weak amplitude collective expansion and contraction dynamics, which becomes more prominent as the dipolar gas enters the turbulent regime. This is due to the gradual melting of the supersolid crystals which are initially elongated along the axial direction [see also Fig. 1 in the main text]. The collective dynamics is, of course, less violent compared to the planar motion, precisely due to the quasi-2D setting. Interestingly, the periodic driving causes localized density modulations around $z = 0$, leading to hump-like structures at small length scales, see Fig. S1(a) at $t = 773$ ms. This is further corroborated by the corresponding momentum distribution $n(k_z,t) = \int dk_x dk_y\ |\mathcal{F}[\Psi](k_x,k_y,k_z,t)|^2$, with $\mathcal{F}[\Psi]$ denoting the Fourier transform of the 3D wavefunction [Fig. S1(b)]. As time progresses, the large k_z momentum tails become significantly populated (as an imprint of the localized density humps in $n(z,t)$), evincing energy transfer processes in the axial direction as well.

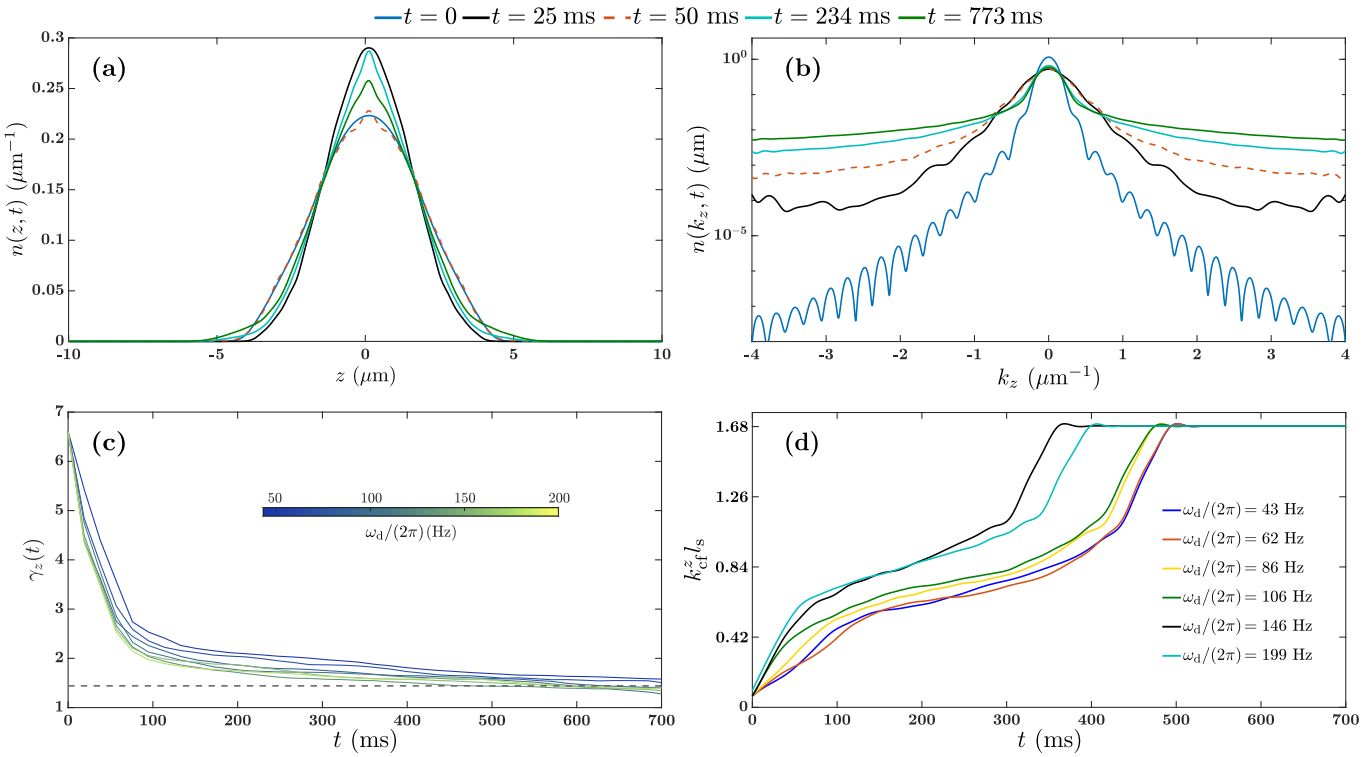

FIG. S1. (a) Integrated density snapshots (see legend) along the axial z-direction upon dynamically crossing the supersolid-to-superfluid transition in a periodic manner with $\omega_d/(2\pi) = 127$ Hz. As it can be seen, the density dynamics in the z-direction is basically restricted to a weak amplitude collective motion. (b) The corresponding momentum distribution reveals relatively enhanced tails, reflecting the presence of the small length scale density fluctuations [panel (a)] and signaling the transfer of energy in the z direction. (c) Scaling exponents, $\gamma_z(t)$, quantified through the algebraic reduction of $n(k_z,t)$ at large momenta. Saturation occurs close to 1.4 (dashed line) over a large range of driving frequencies (see legend). (d) Time-evolution of the cascade front, k_{cf}^z, capturing the energy transfer in the z direction.

To further understand this energy transfer, we inspect the high momentum tails of $n(k_z,t)$, which display an

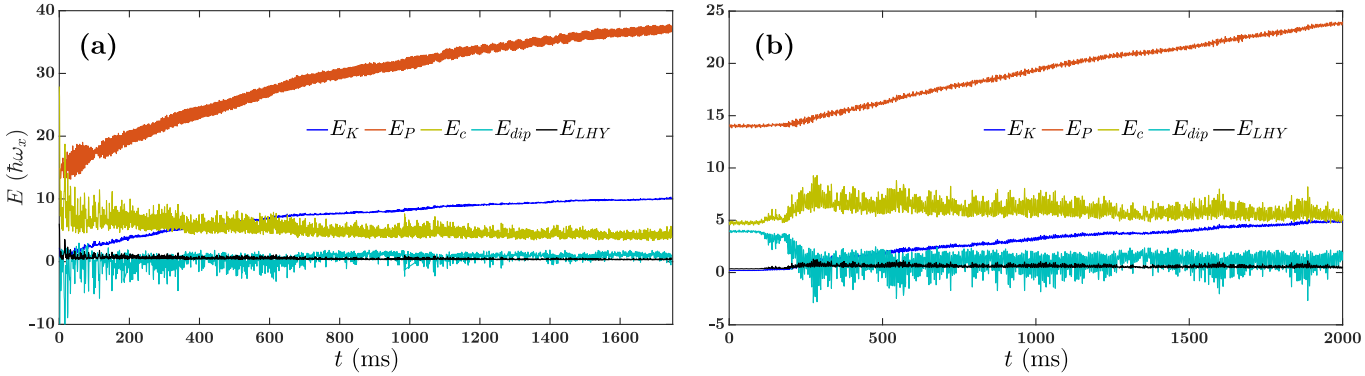

FIG. S2. Individual energy contributions (see legend and text) in the case of the (a) supersolid-to-superfluid and (b) superfluid-to-supersolid dynamical crossings. The kinetic energy increases over time in both cases, evincing the development of wave turbulence. All interaction contributions show a decreasing tendency in the course of the evolution, while the potential energy dominates due to spreading of the density distribution in the plane. The used driving frequencies correspond to (a) $\omega_{\rm d}/(2\pi) = 127$ Hz and (b) $\omega_{\rm d}/(2\pi) = 85$ Hz.

algebraic scaling at large momenta, $n(k_z \gg 1, t) \simeq k_z^{-\gamma_z(t)}$. The associated exponent, $\gamma_z(t)$, saturates at long evolution times [Fig. S1(c)] close to $\gamma_z \simeq 1.4$ [see also the dashed line]. To compare the exponent with the one resulting from the planar dynamics, we employ the line-of-sight integrated distribution, $n_x(k_x, t) = \int dk_y\ n(\mathbf{k}, t)$. The corresponding exponents, γ_x, i.e. $n_x(k_x \gg 1, t) \simeq k_x^{-\gamma_x(t)}$, tend asymptotically to ≈ 1.57. They are reduced as compared to the ones reported in the main text, $\gamma \approx 2.57$, due to the integration [S1]. The discrepancy between γ_x and γ_z reveals that the turbulent cascade develops differently in the plane compared to the z-direction. Such a difference can be attributed to the 2D crystal structure of the dipolar gas in the supersolid phase, which results in anisotropic momentum distributions during the turbulent cascade. However, the origin of the saturated γ_z value remains an open question for future investigations, aiming to investigate the impact of different dimensionalities and their crossover on the observed scaling exponents. Similarly to the planar dynamics, a cascade front $k_{\rm cf}^z$ in the axial direction can be defined, stemming from the compensated spectra $n(k_z, t)(k_z l_{\rm s})^{\gamma_z}$, where γ_z is the saturated exponent. The cascade front [Fig. S1(d)] clearly indicates a direct energy cascade. However, the temporal behavior of $k_{\rm cf}^z$ deviates significantly from the power law behavior observed in the case of the planar dynamics.

SUPPLEMENTARY NOTE 2: INTERPLAY OF ENERGY CONTRIBUTIONS

The onset of wave turbulence reported in the main text for dipolar gases signifies the transfer of energy from large to small length scales. This is clearly illustrated by the extended high momentum tails of the momentum distribution presented in Fig. 2(a) in the main text. Such an energy transfer occurs primarily due to single particle excitations, and thus the kinetic energy, E_K, continuously increases. This mechanism can be readily testified by inspecting Fig. S2 depicting the evolution of the participating energy contributions for both the supersolid-to-superfluid and the superfluid-to-supersolid dynamical transitions using the periodically modulated scattering length protocol discussed in the main text. Notably, E_K starts to increase from early evolution times when the system is initialized in the supersolid phase [Fig. S2(a)], a behavior that is attributed to the faster onset of wave turbulence displayed by supersolids.

Apart from the kinetic energy, the potential term, E_p, shows an increasing tendency and in fact it is the most dominant one. In the turbulence regime, the dipolar gas becomes substantially excited and expanded across the plane resulting in a prevalent E_p contribution. This is accompanied by a decrease in the energy due to dipolar interactions, E_{dip}. Moreover, the energy associated to the beyond mean-field correction term, E_{LHY}, is negligible at late evolution times. Its contribution is significant only at the initial time instants for the supersolid-to-superfluid crossing [Fig. S2(a)]. This occurs since the initial state (supersolid) exhibits high density crystal peaks [see also Fig. 1(a) in the main text]. Subsequently, the crystals melt and so E_{LHY} rapidly diminishes. Furthermore, the energy attributed to contact interactions, E_c, features a small decreasing tendency, especially at large evolution times ($t > 800$ ms in Fig. S2), since atoms in the turbulent regime tend to slightly spread apart.

SUPPLEMENTARY NOTE 3: ABSENCE OF TURBULENCE FOR DRIVING WITHIN THE SAME PHASE

In the main text, it is argued that, regardless of the initial state (SF, SS, or droplet), when the dipolar gas is periodically driven across one of the resulting phase transitions, it exhibits wave turbulence in the later stages of the evolution. Here, we demonstrate that employing sufficiently small driving amplitudes, $a_{\rm f} - a_{\rm i}$, which ensure that the dipolar gas remains in the same phase dynamically, prevents the manifestation of a turbulent response, irrespective of the initial state. To substantiate our argument we present the nonequilibrium dynamics when the dipolar BEC is initiated either in the SF or the SS state and it is subsequently under the influence of a sinusoidally modulated 3D scattering length with an amplitude that does not exceed any relevant phase boundary. The density snapshots of the driven dipolar gas are presented in Fig. S3. Starting from a SS state characterized by $a_{\rm i} = 89\ a_0$ we observe that, upon driving with $a_{\rm f} = 91\ a_0$ and $\omega_{\rm d} = 2\pi \times 127$ Hz, only relatively small amplitude density undulations develop on top of the original hexagonal structure distorting the background SF but not the droplet arrangement, see the integrated density profiles depicted in Fig. S3(a)-(c). This response remains the same for longer timescales and holds for different driving frequencies that we have checked.

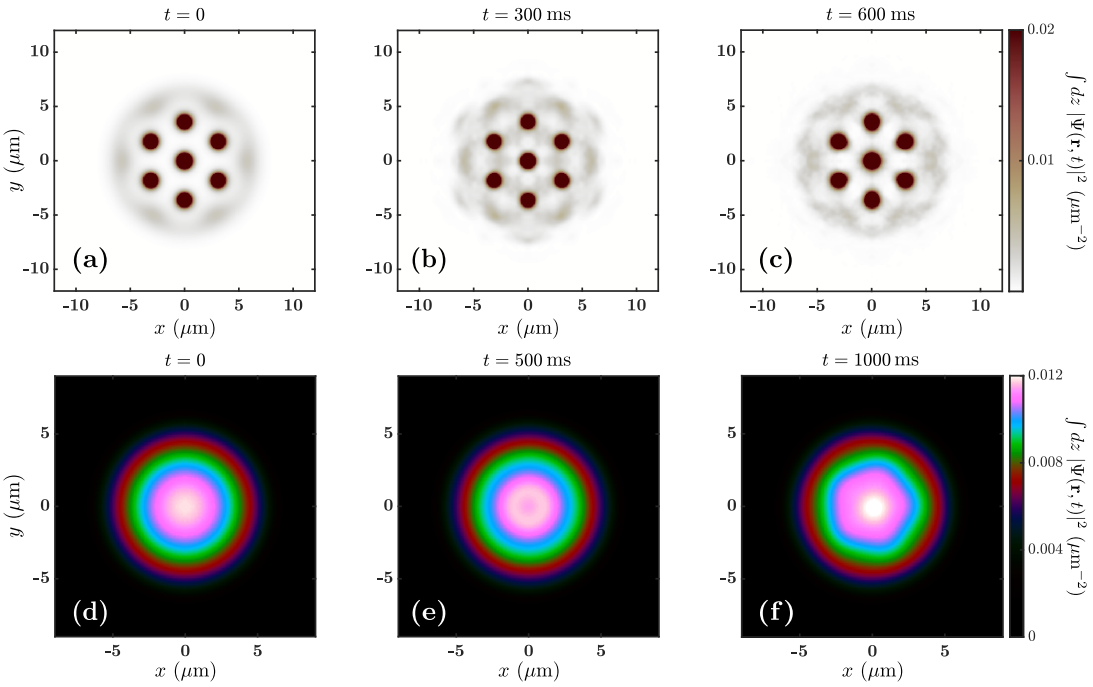

FIG. S3. Absence of wave turbulence for a dipolar gas driven within the same phase. Density snapshots (integrated along the axial direction) across the x-y plane for an initial (a)-(c) SS with $a_{\rm i} = 89\ a_0$ and (d)-(f) a SF at $a_{\rm i} = 98\ a_0$. Evidently, the SS features a distorted background while the SF performs a collective motion. The driving amplitude, $|a_{\rm f} - a_{\rm i}| = 2\ a_0$, is relatively small in both cases such that the underlying ground state phase boundary is not dynamically crossed. The used driving frequencies are $\omega_{\rm d} = 2\pi \times 127$ Hz and $\omega_{\rm d} = 2\pi \times 85$ Hz for the SS and SF respectively.

Turning to a driven dipolar SF with $a_{\rm i} = 98\ a_0$, $a_{\rm f} = 96\ a_0$ and $\omega_{\rm d} = 2\pi \times 85$ Hz, illustrated in Fig. S3(d)-(f), it can be seen that collective motion of the background occurs in the form of an isotropic breathing mode. This is accompanied by signatures of developing bulk structures such as the pentagon pattern appearing in Fig. S3(f). The spontaneous generation of such patterns is another interesting venue for future research in terms of exploiting parametric instabilities [S2, S3]. Let us finally note that when the driving amplitude $a_f - a_i$ is small but sufficient to cross the phase boundary, wave turbulence characteristics develop at long evolution times (not shown). The onset of turbulence is slower compared to the case where the driving amplitude is large.

SUPPLEMENTARY NOTE 4: TURBULENCE IN THE PRESENCE OF DISSIPATION

As demonstrated in the main text, energy is transported to smaller length scales by means of nonlinear wave interference resulting in wave turbulence. Additionally, we have considered a fully condensed gas without any damping channels. In the following, we study the emergent non-equilibrium dynamics by including a phenomenological damping term, κ, to the extended Gross-Pitaevskii equation [S4–S7],

$$(\mathrm{i}-\kappa)\hbar\partial_t\Psi(\mathbf{r},t)=\left[-\frac{\hbar^2}{2m}\nabla^2+V(\mathbf{r})+\frac{4\pi\hbar^2 a}{m}\left|\Psi(\mathbf{r},t)\right|^2+\int d\mathbf{r}'\ U_{\rm dd}(\mathbf{r}-\mathbf{r}')\left|\Psi(\mathbf{r}',t)\right|^2+f(\epsilon_{\rm dd})\left|\Psi(\mathbf{r},t)\right|^3\right]\Psi(\mathbf{r},t). \tag{S1}$$

The above model accounts for collisions of condensed atoms with those occupying the thermal fraction. Such processes lead to the damping of excitations in the condensed portion without any accompanied particle loss. The damping factor κ usually depends on temperature, and is inversely proportional to the relaxation time of the dipolar BEC [S8]. The significance of κ becomes apparent when the above equation is expressed in the hydrodynamical formalism, where $\hbar\kappa/(2m)$ plays the role of viscosity, dubbed the kinematic quantum viscosity [S9].

To develop an understanding on how dissipation affects the onset of turbulence for the SS-to-SF dynamical crossing, we consider κ in the range $[10^{-5},10^{-2}]$. The influence of damping can be readily seen by contrasting the momentum distributions in Fig. S4(a),(b). A larger κ leads to the decay of high momentum excitations of the system that would otherwise be responsible for carrying energy to small length scales in the direct turbulent cascade. Instead, the high momentum tail of $\tilde{n}(|\mathbf{k}|,t)$ is highly suppressed, and even at large evolution times, the distribution remains close to the initial one. Such an equilibration process is observed also in the time evolution of the extracted exponent at large momenta [Fig. S4(c)]. For $\kappa=10^{-5}$, which represents adequately small dissipation, the exponent quickly decreases close to the value obtained in the absence of dissipation. For a larger $\kappa=10^{-4}$, $\gamma(t)$ still saturates, but to a plateau whose value is larger than what is anticipated for weak wave turbulence. As the damping term increases further, $\gamma(t)$ fluctuates close to its initial value.

SUPPLEMENTARY NOTE 5: SIMULATION DETAILS

To numerically tackle the ground state properties and the nonequilibrium dynamics of the considered quasi-2D dipolar gas we simulate the extended Gross-Pitaevskii equation (1) provided in the main text. For numerical convenience it is casted in a dimensionless form. Specifically, space and time scales are expressed in units of the harmonic oscillator length $a_{\rm ho}=\sqrt{\hbar/(m\omega_x)}$ and ω_x^{-1} respectively. Moreover, the 3D wave function is rescaled according to $\Psi(\mathbf{r},t)=\sqrt{N/a_{\rm ho}^3}\Psi'(\mathbf{r}',t')$, where the prime quantities refer to dimensionless ones. Note that this rescaling implies that the Ψ' wave function is normalized to unity, i.e. $\int d\mathbf{r}'\ \left|\Psi'(\mathbf{r}',t')\right|^2=1$. Additionally, the three-dimensional space is discretized in a uniform cubic grid of $512\times512\times128$ points along the x, y and z directions respectively with spatial discretization $\delta x=\delta y=0.08a_{\rm ho}$ in the plane and $\delta z=0.2a_{\rm ho}$ in the axial direction. The time step of the numerical integrator is set to $\delta t=10^{-4}/\omega_x$ for both the imaginary and real time propagation of Eq. (1) in the main text. These are carried out by means of the split-step Crank-Nicolson numerical scheme [S10, S11]. In order to deal with the divergent behavior of the integrand present in the dipolar interaction integral [Eq. (1) in the main text], we utilize the convolution theorem [S12, S13]. In this way, the interaction integral is expressed as the inverse Fourier transform of the product of Fourier transforms of the dipolar interaction and wave function respectively. Therefore, the integral in Eq. (1) of the main text becomes numerically stable, without the need of any regularization scale.

To numerically obtain the exotic ground states of the dipolar gas, namely the SF, SS and droplet phases, the following initial ansatz is utilized

$$\Psi'(x',y',z',t=0)=\mathcal{A}\left[\cos\left(\frac{2\pi x'}{3}\right)+\cos\left(\frac{\pi x'}{3}+\frac{\pi y'}{\sqrt{3}}\right)+\cos\left(-\frac{\pi x'}{3}+\frac{\pi y'}{\sqrt{3}}\right)\right]^4 \mathrm{e}^{-0.01[(x')^2+(y')^2]-(\omega_z/\omega_x)(z')^2/2}, \tag{S2}$$

with $\mathcal{A}$ being a normalization constant. This ansatz is particularly tailored for capturing the six-fold symmetry of the cylindrically symmetric SS configurations [S14]. During every step of the imaginary time propagation, the dimensionless wave function is rescaled, $\Psi'\to\Psi'/\left\|\Psi'\right\|$, where $\left\|\Psi'\right\|\equiv\int d\mathbf{r}'\ \left|\Psi'\right|^2$ denotes the norm, ensuring that the normalization is preserved. The ground state is identified by requiring that the relative difference between the wave functions in two consecutive time steps of the imaginary time propagation is lower than 10^{-4} and the corresponding

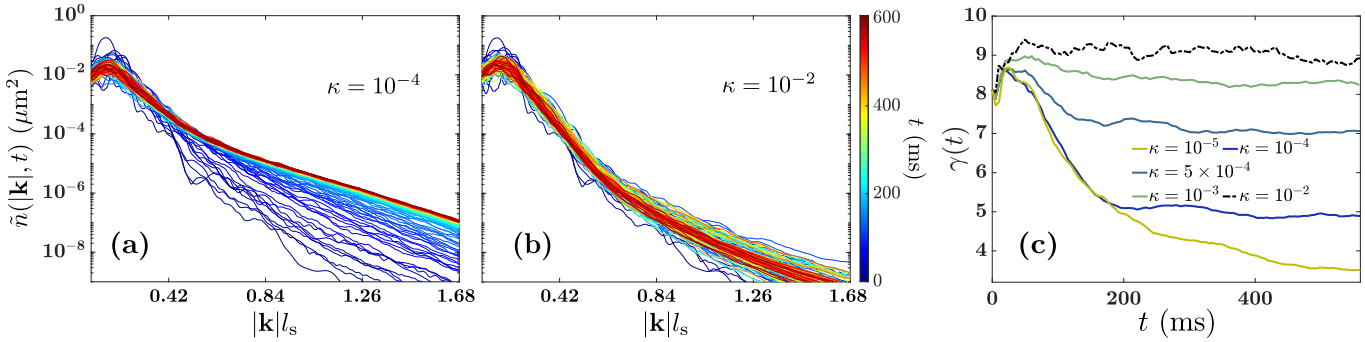

FIG. S4. Emergence of quasi-steady state at long evolution times in the presence of dissipation. Dynamics of the momentum distributions of an initial SS ($a_i = 89\ a_0$) undergoing through the SS-to-SF transition with $a_f = 98\ a_0$, $\omega_d = 2\pi \times 127$ Hz and phenomenological damping (a) $\kappa = 10^{-4}$ and (b) $\kappa = 10^{-2}$ respectively. (c) Time evolution of the exponents at large momenta for different phenomenological damping terms (see legend). A large κ facilitates the suppression of the large momentum tails, and hence it leads to significantly elevated exponents at late time instants.

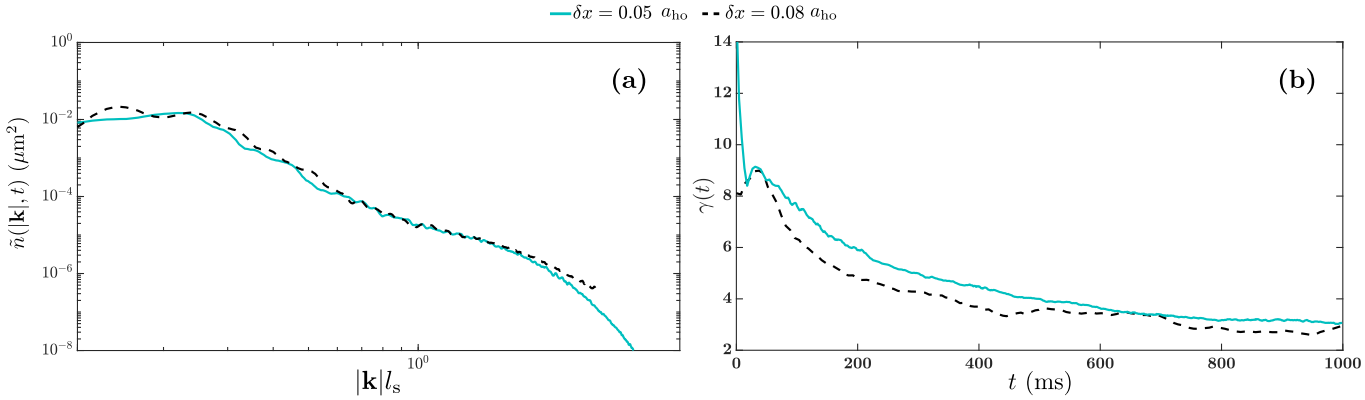

FIG. S5. Comparison of (a) the azimuthally averaged momentum distribution at $t = 1000$ ms and (b) the scaling exponent dynamics for different spatial discretizations (see legend) of the numerical simulations. Here, the supersolid-to-superfluid transition is dynamically crossed with $a_i = 89\ a_0$, $a_f = 98\ a_0$ and $\omega_d/(2\pi) = 127$ Hz.

energy deviations do not exceed 10^{-8}. This state is subsequently employed for the real time dynamics of Eq. (1) in the main text. Our spatial and time (δt) discretizations are chosen such that $(\delta t)^2 < \delta x \delta y$ holds and as a consequence the real time dynamics is accurately simulated. Namely, the total particle number and energy are numerically conserved within the order of 10^{-6} in the course of the evolution.

To further support the persistence of the turbulent characteristics discussed in the main text, we have performed simulations for smaller spatial discretizations, $\delta x = \delta y = 0.05\ a_{ho}$ [Fig. S5]. As such, larger momenta can now be accessed compared to the case with $\delta x = \delta y = 0.08\ a_{ho}$ [compare the two lines in Fig. S5(a)] employed in the main text. The angularly averaged momentum distribution remains almost un-affected as can be seen in Fig. S5(a), referring to the supersolid-to-superfluid transition, at least for the momenta that can be accessed with larger spatial discretizations. Importantly, the exponent $\gamma(t)$ remains the same at long evolution times, saturating at the same value [Fig. S5(b)]. This value can now be extracted by fitting to a larger interval in momentum space, i.e. $|\mathbf{k}|\, l_s \in [0.6, 1.9]$, due to the access to larger $|\mathbf{k}|$ compared with the case pertaining to $\delta x = \delta y = 0.08\ a_{ho}$. Discrepancies between the exponents stemming from the two different spatial discretizations occur mostly during the early evolution times. This is due to the suppressed high momentum tails (large $\gamma(t)$), which are sensitive to the grid spacing. Similar conclusions can be drawn from the superfluid-to-supersolid phase transition. Summarizing, it is possible to infer the robustness of the observed dynamical response for different spatial discretizations.

SUPPLEMENTARY REFERENCES

[S1] N. Navon, A. L. Gaunt, R. P. Smith, and Z. Hadzibabic, Nature **539**, 72 (2016).

[S2] K. Kwon, K. Mukherjee, S. J. Huh, K. Kim, S. I. Mistakidis, D. K. Maity, P. G. Kevrekidis, S. Majumder, P. Schmelcher, and J.-y. Choi, Phys. Rev. Lett. **127**, 113001 (2021).
[S3] N. Liebster, M. Sparn, E. Kath, K. Fujii, S. Görlitz, T. Enss, H. Strobel, and M. K. Oberthaler, arXiv e-prints , arXiv (2023).
[S4] S. Choi, S. A. Morgan, and K. Burnett, Phys. Rev. A **57**, 4057 (1998).
[S5] L. Pitaevskii, Sov. Phys.—JETP **8**, 282 (1959).
[S6] T. Bland, E. Poli, C. Politi, L. Klaus, M. Norcia, F. Ferlaino, L. Santos, and R. Bisset, Phys. Rev. Lett. **128**, 195302 (2022).
[S7] E. B. Linscott and P. B. Blakie, Phys. Rev. A **90**, 053605 (2014).
[S8] N. P. Proukakis, G. Rigopoulos, and A. Soto, arXiv:2407.20178 (2024).
[S9] A. S. Bradley and B. P. Anderson, Phys. Rev. X **2**, 041001 (2012).
[S10] J. Crank and P. Nicolson, in *Math. Proc. Camb. Philos. Soc.*, Vol. 43 (Cambridge University Press, 1947) pp. 50–67.
[S11] X. Antoine, W. Bao, and C. Besse, Comput. Phys. Commun. **184**, 2621 (2013).
[S12] G. B. Arfken and H.-J. Weber, *Mathematical methods for physicists* (Academic Press Orlando, FL, 1972).
[S13] K. Góral and L. Santos, Phys. Rev. A **66**, 023613 (2002).
[S14] D. Baillie and P. B. Blakie, Phys. Rev. Lett. **121**, 195301 (2018).